Materials Advances

ROYAL SOCIETY OF CHEMISTRY

PAPER

View Article Online
View Journal | View Issue

Cite this: *Mater. Adv.*, 2024, 5, 5802

Hydrophobized lignin nanoparticle-stabilized Pickering foams: building blocks for sustainable lightweight porous materials†

Tao Zou, ‡[ab] Erfan Kimiaei, ‡[a] Zahra Madani,[c] Muzaffer A. Karaaslan,[b] Jaana Vapaavuori,[c] Johan Foster,[d] Scott Renneckar[b] and Monika Österberg *[a]

Pickering particles play an essential role in stabilizing Pickering foams that can be utilized as templates for making lightweight porous materials for thermal insulation purposes. With the shift from petroleum to renewable-source-derived materials, particles synthesized from biomass are emerging but are typically too hydrophilic to function as Pickering particles in foams. Here, we report the hydrophobization of lignin nanoparticles (LNPs) by adsorption of an oppositely charged surfactant for air-in-water Pickering foam stabilization. The surface tension and complex viscoelasticity of the aqueous dispersions were tunable by varying the concentration of LNPs and the adsorption ratio of hexadecyltrimethylammonium bromide (CTAB) onto LNPs, which were systematically studied with the pendant drop technique (DPT). Under the optimum conditions, the achieved air-in-water Pickering foams were remarkably stable against coalescence and coarsening, *i.e.*, the bubble size distribution remained unchanged over 30 days. We further utilized the Pickering foams as templates for making dry lightweight composite foams with the introduction of cellulose nanofibrils (CNFs). The closed-cell composite foams, with lignin as the major component, exhibited good thermal insulation properties and mechanical properties that were comparable to commercial rigid polyurethane (PU) foams. We envision that the renewable Pickering particles could find applications in many other areas beyond the templates for porous materials such as enhanced oil recovery.

Received 20th March 2024,
Accepted 27th May 2024

DOI: 10.1039/d4ma00295d

rsc.li/materials-advances

Introduction

Pickering foams are biphasic wet foams stabilized by particles.[1] Pickering foams are stable against coalescence (film rupture) and coarsening (diffusion of gas molecules from small bubbles to large bubbles due to differences in Laplace pressure, also known as Ostwald ripening) as the particles can strongly adsorb at the gas–liquid interface. The energy needed to remove the particles from the interface can reach thousands of $\kappa_B T$ (κ_B and T denote Boltzmann constant and temperature, respectively), which is three orders of magnitude higher than for conventional surfactants.[1,2] As a consequence, Pickering foams have been widely used in various applications such as food,[3] froth flotation of minerals,[4] enhanced oil recovery,[5] and as precursors for the production of low-density and porous materials.[6,7]

Traditionally, inorganic and synthetic polymeric particles such as silica nanoparticles,[8] alumina particles,[9] and polystyrene particles,[10] have been mainly studied for Pickering foam stabilization. These particles normally undergo partial hydrophobization to function as Pickering particles. In recent years, there has been growing interest in particles derived from biological origin for Pickering foam stabilization.[11] Compared with inorganic or synthetic polymeric particles, biomass-derived particles offer the advantages of renewability, biodegradability, and biocompatibility, making them favorable for circular economy and a sustainable society. Among these particles, cellulosic particles made from cellulose or cellulose derivatives have been mostly reported.[11] Alike inorganic and synthetic polymeric particles, partial hydrophobization of cellulosic particles is required for them to function as Pickering particles. This has been achieved either by etherification or esterification of cellulose and further conversion into spherical particles,[12,13] or by physical adsorption

[a] *Department of Bioproducts and Biosystems, School of Chemical Engineering, Aalto University, Espoo, Finland. E-mail: monika.osterberg@aalto.fi*
[b] *Department of Wood Science, University of British Columbia, 2424 Main Mall, Vancouver, British Columbia V6T 1Z4, Canada*
[c] *Department of Chemistry and Materials Science, School of Chemical Engineering, Aalto University, Espoo, Finland*
[d] *Department of Chemical and Biological Engineering, University of British Columbia, CHBE 421, 2360 East Mall, Vancouver V6T 1Z3, British Columbia, Canada*

† Electronic supplementary information (ESI) available. See DOI: https://doi.org/10.1039/d4ma00295d

‡ These authors have contributed equally to this work and are co-first authors.

of oppositely charged surfactant or hydrophobic cellulose onto cellulose nanofibrils (CNFs) or cellulose nanocrystals (CNCs).[7,14]

Compared with cellulosic particles, lignin nanoparticles (LNPs), an emerging biomass-derived particle made of lignin,[15,16] have not been studied for Pickering foam stabilization. LNPs are typically spherical in shape,[17] which gives them a lower aspect ratio compared to CNFs or CNCs.[18] The aspect ratio also plays a relevant role in Pickering foam stabilization with higher aspect ratio leading to higher foam stability.[19] Lignin, the second most abundant biomass photosynthesized in nature right after cellulose, has been treated as a side stream in the pulp and paper industry.[20,21] Annually, approximately 98% out of 100 million tons of lignin are burnt for energy purposes, causing premature CO_2 emission.[22] Nevertheless, lignin valorization for materials applications has triggered tremendous interest in recent years, not only because of its abundance, and non-competition with food sources, but also due to its attractive properties such as antioxidant and UV blocking properties.[22,23] Over the years, the underutilization of lignin for materials applications has been mainly hindered by the heterogeneous molar mass, molecular structure, and functional groups arising from different plant species and isolation processes.[23] To address this issue, one promising approach is converting lignin to LNPs.[17] Unlike raw lignin, LNPs have a well-defined surface chemistry, large surface area per mass unit, and good dispersibility in water from pH 3 to 10.[17,24] These improved properties enable value-added applications of lignin,[17] including Pickering emulsion stabilization.[25–29] However, to our best knowledge, no efforts have been conducted to utilize LNPs as emulsifiers for Pickering foam stabilization. The underlying reason is that LNPs are too hydrophilic to be used for Pickering foam stabilization, similar to other biomass-derived particles.[30] Besides, generating Pickering foams is more challenging than producing Pickering emulsions due to the former (gas/liquid) exhibiting a higher interfacial energy compared to the latter (liquid/liquid), hence more hydrophobic LNPs are needed. One study reported the combination of LNPs and alpha olefin sulfonate (AOS) for wet foam stabilization and found that the foam exhibited 10 times longer half-life time than the foam stabilized solely by AOS.[31] However, the enhanced stability was not a result of the Pickering effect, but due to the particle congestion in the Plateau borders that slowed down the drainage and bubble coalescence.[32]

In this work, we systematically studied the surface tension and complex viscoelasticity of the aqueous LNP dispersion across a broad range of LNP concentrations (0–5 wt%) and varying the adsorption ratios of Hexadecyltrimethylammonium bromide (CTAB) to achieve optimum conditions for generating Pickering foams. CTAB, a quaternary ammonium cationic surfactant, has been successfully utilized to hydrophobize anionic LAPONITE® and silica particles for Pickering foam stabilization.[33,34] One recent study furthermore showed that CTAB meets the criteria for ready biodegradability without sorbent, and its toxicity can be mitigated when particle sorbents are used.[35] On top of the Pickering foam stabilization, we further demonstrate that the Pickering foam system can be utilized as a template for making lightweight, strong, closed-cell foams with the introduction of cellulose nanofibrils (CNFs).

Experimental

Materials

Softwood kraft lignin (SKL) (Brand name: Biopiva 100) used in this study was isolated from black liquor using LignoBoost technology (UPM, Finland).[36] SKL was well characterized in previous studies,[37,38] it has a sugar content of 0.05 mmol g^{-1}, nominal number-average molecular weight (M_n) and weight-average molecular weight (M_w) of 693 and 4630 g mol^{-1} (determined with gel permeation chromatography using polystyrene sulfonates as standards), respectively. The aliphatic OH, phenolic OH, and carboxyl groups contents were 1.89, 4.05, and 0.38 mmol g^{-1} (determined with ^{31}P NMR), respectively. The cellulose nanofibrils (CNFs) were prepared according to Österberg *et al.*[39] In brief, never dried bleached hardwood kraft pulp fibers were washed into sodium form and then subjected to mechanical disintegration. The mechanical disintegration was performed using an M-110P microfluidizer (Microfluidics, Newton, Massachusetts, USA) by six passes through a series of 400 and 100 μm chambers at 2000 bar. The final obtained CNF suspension had a solid content of 2.1 wt%, which was stored at 4 °C before use. Hexadecyltrimethylammonium bromide (CTAB) (purity ≥98%) was purchased from Sigma-Aldrich. Deionized water was used throughout the experiments. A commercial rigid polyurethane (PU) foam with the brand name FF-PIR PLK was purchased from Finnfoam (Finland).

Preparation of lignin nanoparticles

LNPs were prepared following previously reported method with slight modifications.[26,40] In brief, 15 g of wet SKL (~33 wt% moisture) was dissolved in 500 g of aqueous acetone (75 wt%) under stirring for 4 hours, followed by vacuum filtration through a paper filter (Whatman GF/F, pore size 0.7 μm) to remove the undissolved solids. Afterward, lignin solution was quickly poured into deionized water (1500 g) under vortex-stirring to form LNPs instantly. The LNP dispersion was then subjected to rotary evaporation at 45 °C under reduced pressure to remove acetone and further concentrated to 5–7 wt%. The final aqueous LNP dispersion consisted solely of LNPs dispersed in water.

Hydrodynamic diameter (D_h) and ζ potential analysis

The hydrodynamic diameter (D_h) and ζ potential of the LNPs were determined using a Zetasizer Nano ZS90 instrument (Malvern Instruments Ltd, United Kingdom). Prior to measurement, the LNP dispersion was diluted to 0.01 wt% with deionized water and subjected to bath ultrasonication for 10 minutes. The D_h was obtained at the scattering angle of 90°. The ζ potential measurement were conducted with a dip cell probe using automatic voltage and the ζ potential was calculated using Helmholtz–Smoluchowski equation.[41] Three measurements were recorded for D_h and ζ potential and the average values were used for reporting. The LNPs prepared in this work had the average hydrodynamic diameter D_h (intensity-based) around 140 nm and the ζ potential around −37 mV at pH 5.

Atomic force microscopy (AFM)

The AFM images of LNPs and CNFs were taken with a Multi-Mode 8 AFM equipped with a NanoScope V controller (Bruker Corporation) in tapping mode in ambient air using NCHV-A probes (Bruker). The LNP sample was prepared by dropping 5 μL LNP dispersion (0.01 wt%) on a mica surface followed by ambient drying, while the CNF sample was prepared by spin-coating of CNF dispersion (0.1 wt%) on a silica surface. Image processing (third order plane fit) was performed using Nanoscope Analysis (version 1.5, Bruker).

Surface tension and dilational viscoelasticity

Theory. The pendant drop profile technique (DPT) was adapted for measuring surface tension (γ), dilational viscoelasticity (E), and phase shift (φ).[42–44] The shape of the droplet is defined by the gravity force (which will elongate the droplet) and surface tension (which strives to keep the droplet spherical), hence γ can be calculated from the droplet profile using Young–Laplace equation (detailed equations refer to Stauffer[43] and Yang *et al.*[44]). E is calculated based on the harmonic response of γ to a given harmonic oscillation of the interfacial area A at a low frequency from its equilibrium state, which is expressed as:

$$E = \frac{\Delta\gamma}{\Delta A/A_0} = \frac{\tilde{\gamma}}{\tilde{A}/A_0}e^{i\varphi} \quad (1)$$

where ΔA varies in a harmonic manner (harmonic oscillation of the droplet): $\Delta A = \tilde{A}e^{i2\pi\nu}$ ($\tilde{A}$ is the amplitude and ν is the frequency), $\Delta\gamma$ responses as: $\Delta\gamma = \tilde{\gamma}e^{i(2\pi\nu+\varphi)}$ ($\tilde{\gamma}$ is the amplitude and φ is the phase shift), A_0 is the surface area at equilibrium state of the droplet. $\tilde{\gamma}/(\tilde{A}/A_0)$ is usually reported in the term of complex viscoelastic modulus $|E|$.

At a relative low oscillation frequency, *e.g.*, at 0.1 Hz, $\tilde{\gamma}$ is low for a droplet containing conventional surfactant, as the surfactant can diffuse to/away from the interface that dampens the external area perturbation, thus a relatively low $|E|$ is expected. In contrast, a relatively high $|E|$ is expected for a droplet containing particles at the interface due to strong adsorption, since a high energy is required for the desorption of particles from the interface.[1,45] φ on the other hand reflects how viscoelastic the interface is.

Measuring procedure. γ, $|E|$ and φ of the LNP, CTAB–LNP aqueous dispersions and CTAB aqueous solutions were analyzed on an optical tensiometer (Biolin Scientific Attension Theta) equipped with a pulsating drop module. The dispersion/solution was expensed from a steel tip (diameter of 1.2 mm) forming a pendant drop (8 μL) inside a sealed quartz cuvette covered with parafilm to prevent water evaporation. A high-speed camera started recording the droplet profile as soon as the droplet formed at the recording speed of 5 frames per second. The droplet was allowed to equilibrate for 10 min (dispersion) or 3 min (solution) and then sinusoidal oscillation perturbation was applied to the droplet at the frequency of 0.1 Hz and amplitude of 5% ($\tilde{A}/A_0$) for 1 min, hence 6 cycles of the sinusoidal oscillations were recorded. To ensure data reliability, a deionized water droplet was expensed and the γ was measured at 72 mN m^{-1} before switching to the dispersion/solution. One Attension software was adapted for the data analysis. γ was calculated from the last minute of the droplet profiles during the equilibration, $|E|$ and φ were calculated from the recorded data of 6 cycles of the sinusoidal oscillations. Three parallel measurements were conducted and the average values were used for reporting.

Wet and dry foam preparation

Wet foams stabilized by CTAB–LNPs were prepared by first mixing an aqueous CTAB solution (1 wt%) with a LNP dispersion (5–7 wt%) at different ratios (*e.g.*, 0 to 15 mg g^{-1} CTAB to LNP) by gentle-stirring for 3 hours, followed by foaming using an Ultra-turrax T18 (basic IKA homogenizer) for 3 min at 14 k rpm. Wet foams containing CTAB–LNPs and CNFs were prepared similarly as above with the only difference that CNFs were added into the LNP dispersions right after adding CTAB with a final concentration at 0.7–0.9 wt%. The detailed foam formulations can be found in the ESI† (Table S1 and S2).

The dry foams were prepared by freeze-drying (Labconco, freezone 2.5). Prior to freeze-drying, the wet foams were transferred into a round-shape poly(tetrafluoroethylene) (PTFE) mold (80 mm in diameter and 28 mm in height), followed by freezing at −20 °C in a freezer.

Wet foam characterization

The foamability was illustrated using the foaming index that was calculated according to the following equation:

$$\text{Foaming index (\%)} = 100\% \times (\text{Foam volume/initial liquid volume}) \quad (2)$$

The foam stability was estimated from the change of foaming index over time.

The microstructure of the wet foams was observed with an optical microscope (Leica Zeiss DM750) equipped with Leica imaging software. The captured images were analyzed by ImageJ.

The bubble size distribution and uniformity of the wet foams were determined with a Mastersizer 2000 (Malvern, UK). The refractive indices of the dispersed and continuous phases were set at 1.6 and 1.33, respectively. The wet foams were diluted with deionized water to reach the laser obscuration of 5–10% prior to starting the measurement. The mean droplet diameter was calculated according to volume-based size distribution (d_{43}, De Brouckere Mean Diameter). The uniformity of the size distribution was calculated according to the following equation:

$$\text{Uniformity} = \frac{\sum X_i|d(v,0.5) - d_i|}{d(v,0.5)} \quad (3)$$

where $d(v,0.5)$ is the median diameter in the volume-based distribution, d_i is the diameter in class i, and X_i is the corresponding volume fraction in %. An average of five separate measurements was used for reporting.

Dry foam characterization

The cellular structure of the dry foams was determined using scanning electron microscopy (SEM) (Zeiss Sigma VP, Germany) at an acceleration voltage of 2 kV. Prior to imaging, the samples were deposited with a 4 nm-thick layer of gold–palladium alloy. The images were taken from the cryo-fractured cross-section areas and the top surfaces of the samples. ImageJ was used to analyze the SEM images. About 50 cells per sample were measured to determine the cell size distribution.

The closed-cell content was measured by determining the actual density using gas pycnometer (Quantachrome, USA) according to the ASTM D6226 standard and the following equations.[46]

$$\text{Closed cells (\%)} = 100\% - \text{Open cell (\%)} \quad (4)$$

$$\text{Open cell (\%)} = (\text{actual density} - \text{apparent density})/\text{apparent density} \times 100\% \quad (5)$$

The thermal conductivity measurement was performed on a Hot Disk TPS 2500 S (Sweden). A Kapton sensor (model 5465) was adapted for determining the thermal conductivity. The sensor was placed in between two identical foam slabs (~30 mm × 30 mm × 5 mm) and an extra force (2–3 N) was applied to the foams to ensure good contact. The measurement was performed at a heating power of 7 mW for 5 s at 22 °C. Data points between 1 s and 4 s were selected for the thermal conductivity calculation. Two parallel measurements were conducted, and the average values were used for data reporting. The thermal insulation behavior of the foams (~10 mm thick for LNP-CNF foams, and 5 mm thick for the PU foam) was further analyzed by placing them on a hot copper plate at 120 °C for 1 hour (see the setup in the ESI†). The copper plate (155 mm × 155 mm ×1 mm) was placed on the hot plate to ensure thermal uniformity. An infrared camera (PIR uc 605, 640 × 480 pixels) was used to monitor the temperature change at 1 frame per second. ThermaCAM™ Researcher Pro v2.10 was used for data analysis. For data reporting, a colormap was used to indicate the temperature change between 30 °C and 120 °C. The thermal stability of the foams was analyzed *via* thermogravimetric analysis using a TGA Q500 instrument (TA Instruments, USA). The samples were heated at a heating rate of 10 °C min^{-1} up to 800 °C under a nitrogen atmosphere. The temperature corresponding to the highest rate of degradation was determined by plotting the first derivative of the thermogravimetric curves (DTG).

Compression tests were performed on a universal testing machine (Instron 5944). The samples (~30 mm × 30 mm × 10 mm) were first conditioned for 48 h at 23 °C with a relative humidity of 55%. Next, they were compressed up to 80% strain at a tensile speed of 1 mm min^{-1} under a 2 kN load cell. The compressive strength at 10% and 50% strain was used to compare the samples. The toughness was calculated over the strain from 0 to 80%. At least three samples were measured, and the mean values were used for reporting.

Results and discussion

This work aimed to tune the wetting properties of LNPs by adsorbing oppositely charged surfactants onto their surfaces for creating durable Pickering foams. The Pickering foams were further used as templates for lightweight porous materials aiming at future use for thermal insulation and cushioning applications. A general view of this work is shown in Scheme 1.

To obtain optimal performance in foams, the first step was to fundamentally understand how the surface tension and complex viscoelasticity of the aqueous LNP dispersions were affected by the particle concentrations and adsorption ratios of oppositely charged surfactants.

Hydrophobization of LNPs by adsorption of CTABs for durable Pickering foams

Concentration effect on LNP hydrophobicity. Both concentration and wettability of particles play an essential role in forming stable Pickering foams.[1] We first systematically studied the concentration effect on the surface tension (γ), complex viscoelastic modulus ($|E|$), and phase shift (φ) of the aqueous LNP dispersion. The particles were spherical (Fig. S1, ESI†) with an average hydrodynamic diameter of around 140 nm, as determined using dynamic light scattering. As shown in Fig. 1a, the γ of LNP dispersion decreased from 72 mN m^{-1} to around 50 mN m^{-1} with an increase in LNP concentration from 0 to 5 wt%. The γ decreased rapidly as a function of LNP concentration up to 4 wt%, after that, the γ did not seem to decrease anymore. Meanwhile, the $|E|$ and φ increased from 0 to 230 mM m^{-1} and from 0 to π, respectively. The increase in $|E|$ indicates an increasing accumulation of LNPs at the air–water interface, while the increase in φ suggests a more viscous interface. At 5 wt%, both $|E|$ and φ suggested that the LNPs formed closely packed layers (network structures) at the air–water interface, which made the interface "gel-like" and "inert" to area perturbation. The accumulation of LNPs at the air–water interface at a high concentration can be partially attributed to the protonation of carboxyl groups of LNPs, which renders them more hydrophobic. This is supported by the fact that the increase in proton concentration follows a 0.74 power-law relationship with the increased

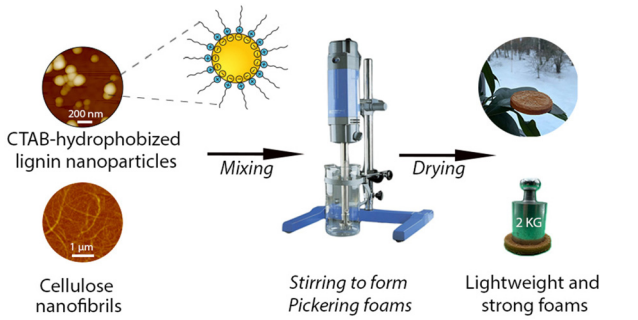

Scheme 1 A general view of this work. The CTAB-hydrophobized LNPs for durable Pickering foam formation with the presence of CNFs, which were further dried for making lightweight and strong solid foams. Note that the schematic drawing of CTAB- coated LNPs is not drawn to scale.

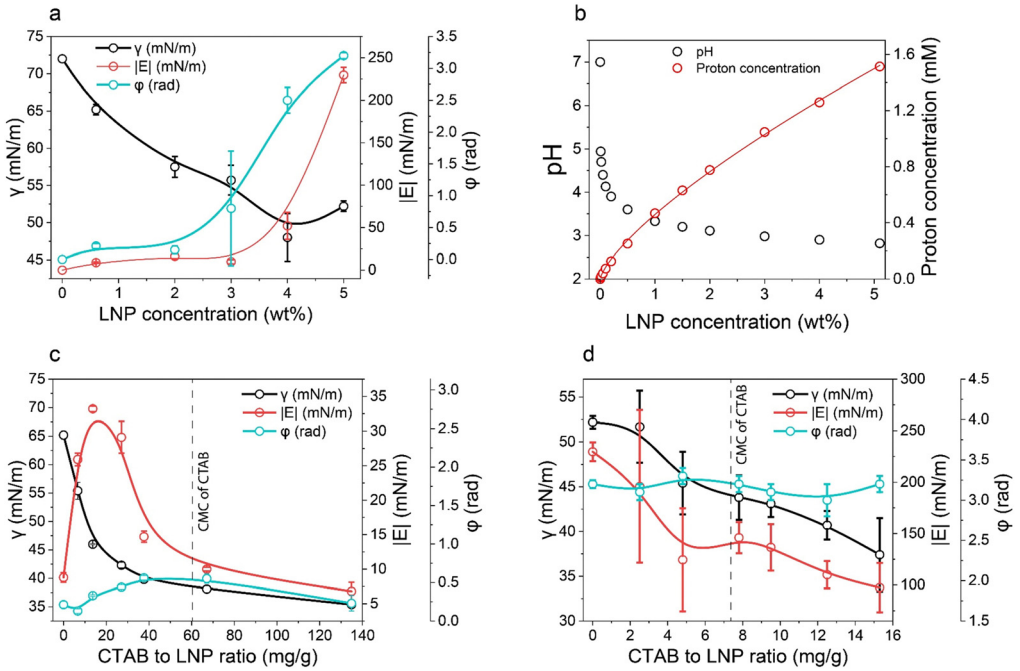

Fig. 1 Wettability of LNPs at different concentrations and adsorption ratios of CTAB. (a) Surface tension (γ), complex viscoelastic modulus ($|E|$), and phase shift (φ) of LNP aqueous dispersions plotted against LNP concentration. (b) pH and proton concentration of LNP aqueous dispersions as a function of LNP concentration. Proton concentration was calculated based on the pH data. Fitting function for proton concentration follows $y = 0.46 \times 0.74$. (c) and (d) γ, $|E|$, and φ of CTAB–LNP aqueous dispersions at the LNP concentrations of 0.6 wt% and 5 wt%, respectively (eqn (1)). The dashed lines denote the critical micelle concentration (CMC) of CTAB in water. Note that the lines in a, c, and d are only added as guides for the eyes.

LNP concentration (Fig. 1b). If there was no change in level of protonation of the carboxyl groups, the proton concentration should increase linearly with the increase of LNP concentration. While comparing our findings with the literature, Stocco *et al.* has previously reported a decrease in γ and increase in $|E|$ with increasing particle concentration for partially silanized silica nanoparticles using the same measuring method.[45]

CTAB adsorption effect on LNP hydrophobicity. An increase in LNP concentration resulted in a decrease in surface tension. However, even at 5 wt%, the LNPs alone were not sufficiently hydrophobic to stabilize a durable Pickering foam, as will be discussed later. Theoretically, the highest stability of Pickering foam is achieved when the interactions of the particles with air and water are equally strong.[1] Therefore, we next studied the effect of CTAB to LNP ratio on γ, $|E|$ and φ at a low (0.6 wt%) and high (5 wt%) LNP concentration. We expected that the adsorption of CTAB on LNPs would further improve the hydrophobicity of the particles. At 0.6 wt% LNPs, γ decreased with an increase in the CTAB to LNP ratio (Fig. 1c). However, $|E|$ initially increased and then decreased, reaching the highest modulus of 33 mN m^{-1} at a CTAB to LNP ratio of 14 mg g^{-1}. This is because CTAB first formed a monolayer on the LNP surface driven by entropy gain due to the release of both counterions into the aqueous phase, rendering the particles more hydrophobic and causing the diffusion of CTAB–LNPs to the air–water interface.[32,33,47] At 14 mg g^{-1} CTAB to LNPs, the particles reached the isoelectric point (IEP) and became the most hydrophobic, and thus covered most of the air–water interface (unfortunately the IEP could not be precisely measured by electrophoretic method when the particle concentration was above 0.2 wt% (Fig. S2a, ESI†)). Further increase in CTAB concentration made the LNPs positively charged due to the formation of CTAB micelles on the LNP surfaces, rendering the LNPs less hydrophobic and causing them to diffuse away from the interface, and the vacancy was dynamically refilled by the free CTAB molecules.[32] As a result, after the addition of 14 mg g^{-1} CTAB–LNPs, $|E|$ decreased and γ further reduced. The assumption that CTAB formed micelles on LNPs at a ratio above 14 mg g^{-1} was based on literature findings. Kedzior *et al.* previously reported that CTAB formed micelles on the acid-form CNCs and bilayers on the sodium-form CNCs at 0.5 times of CTAB critical micelle concentration (CMC), as revealed by colloid-type AFM.[48] In this study, the LNPs were in acid-form and the CTAB reached its CMC of ~1 mM at the CTAB to LNP ratio of 60.7 mg g^{-1} (see Fig. S2b and Fig. 1c, ESI†). The transition of the particle surface charge from negative to positive with the increase of CTAB to LNP ratio was supported by the ζ potential results determined at a relatively low particle concentration (0.1 and 0.2 wt%) (Fig. S2a, ESI†). In addition, the low φ values ($<0.2\pi$) indicated that the change in γ was in phase with the change in the droplet surface area (A), suggesting that the particles formed a monolayer at the air–water interface. For comparison, we also measured the γ and $|E|$ of the aqueous droplets at the same CTAB concentrations without LNPs. In this series, all the measured $|E|$ were under 10 mN m^{-1} (Fig. S2b, ESI†), supporting the fact that the high

$|E|$ detected at 14 mg g^{-1} CTAB–LNPs was due to the strong adsorption of the CTAB–LNPs at the air–water interface. Previously maximum hydrophobicity at IEP has been reported for the adsorption of CTAB molecules onto oppositely charged LAPONITE® particles as determined with contact angle and electrophoretic measurements.[33]

Unlike the results observed with 0.6 wt% LNPs, at 5 wt% LNPs, an increase in the CTAB to LNP ratio resulted in a decrease in both γ and $|E|$, and no obvious change in φ around π (Fig. 1d). The decrease in γ was expected and the reason could be similarly explained as for the CTAB adsorption onto LNPs at a low LNP concentration (0.6 wt%). However, in contrast to the situation for 0.6 wt% LNPs, the maximum $|E|$ corresponding to the highest hydrophobicity and IEP was not observed at 5 wt% of LNPs. The relatively high $|E|$ and the φ around π reflected closely-packed particles at the air–water interface, regardless of the CTAB amount. This might hinder the observation of the maximum $|E|$. Nevertheless, we could estimate that the IEP for 5 wt% LNPs should be less than 14 mg g^{-1} since a higher LNP concentration corresponded to a lower number of dissociated carboxyl groups per particle due to the protonation effect. In fact, the foaming results discussed in the next paragraph indirectly suggested an IEP of 5 mg g^{-1} for CTAB–LNPs at 5 wt% LNPs.

Wet Pickering foams. For producing stable Pickering foams, it is essential to know the IEP of the CTAB–LNPs as it corresponds to the highest hydrophobicity of the particles.[32] As expected, in our foaming experiments, we observed that, for 0.6 wt% LNPs, the most stable foam was formed when stabilized by CTAB–LNPs around the IEP (14 mg g^{-1} CTAB–LNPs). This was indicated by the slowest growth of the mean bubble area compared to foams stabilized by CTAB–LNPs at lower or higher ratios, or foams stabilized with pure CTAB (Fig. S3, ESI†). However, the same results also indicated that the CTAB–LNP concentration at 0.6 wt% was too low to stabilize a foam for several days. A high $|E|$ is a necessity for the formation of durable Pickering foams.[45]

Therefore, we focused on the Pickering foam formation at 5 wt% LNPs. We found that the initial foaming index increased from 207% to 327% with an increased CTAB–LNP ratio from 0 to 15 mg g^{-1} (Fig. 2a and b), indicating improved foamability. Interestingly, the foam stability first improved and then decreased, and the most stable foam was stabilized by 5 mg g^{-1} CTAB–LNPs, as indicated by the smallest change in the foaming index over 30 days (Fig. 2b). Note that the decrease in the foaming index during the first half hour was caused by creaming effect. In contrast, the foams stabilized by the neat LNPs, 12.5 or 15 mg g^{-1} CTAB–LNPs were significantly weaker and completely vanished after 24 hours (Fig. 2a, b and Fig. S4, ESI†). In case of the neat LNPs, the particles were not sufficiently hydrophobic to make the foam durable. For the 12.5 or 15 mg g^{-1} CTAB–LNPs, we speculate that only the free

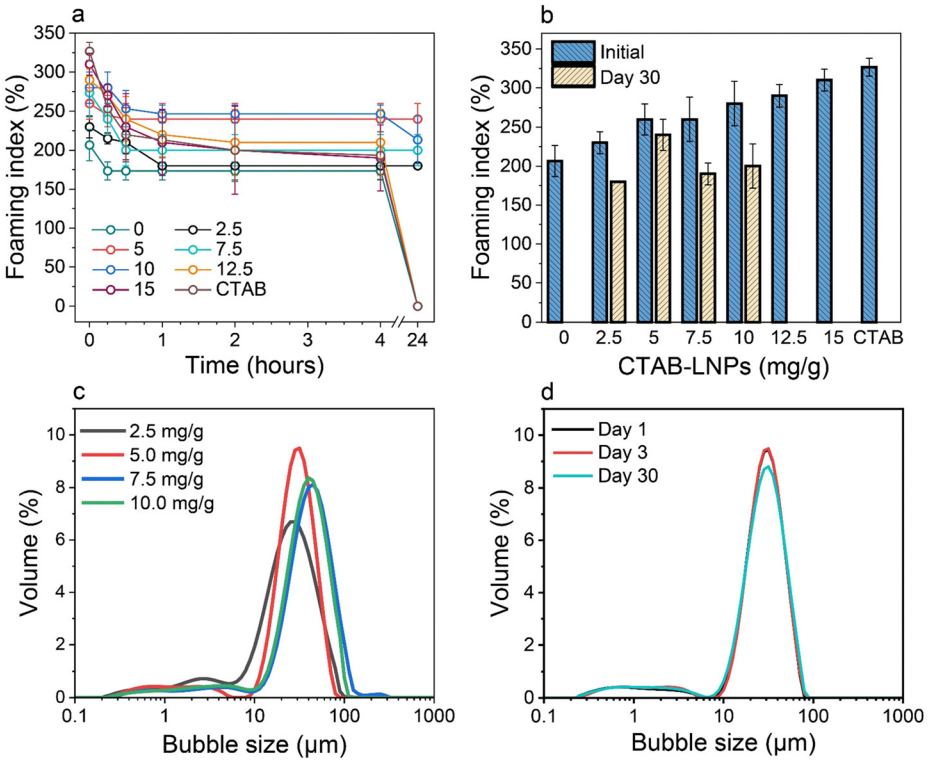

Fig. 2 Effect of CTAB to LNP ratio on foamability (eqn (2)) and foam stability at the fixed LNP concentration of 5 wt%. (a) Foaming index over 24 hours for the foams stabilized by the CTAB–LNPs (0–15 mg g^{-1}) and the neat CTAB. (b) Initial foaming indices (right after foaming) and foaming indices after 30 days. (c) Bubble size distributions of the Pickering foams stabilized by CTAB–LNPs (2.5–10 mg g^{-1}), measured 3 days after foaming. (d) Bubble size distributions of the 5 mg g^{-1} CTAB–LNP-stabilized foam on day 1, 3, and 30 after foaming.

Table 1 Mean bubble size distribution and uniformity (eqn (3)) of the wet foams stabilized by CTAB–LNPs (5 wt%) at the ratios from 2.5 to 10 mg g^{-1}, measured three days after foaming

CTAB to LNP ratio (mg g^{-1})	Mean bubble size (μm)	Uniformity
2.5	25 ± 3	0.6
5	28 ± 1	0.4
7.5	42 ± 1	0.5
10	37 ± 2	0.5

CTAB molecules adsorbed to the air–water interfaces. Since CTAB reached its CMC at 7.2 mg g^{-1} CTAB–LNPs (Fig. 1d), there was likely excess CTAB in the aqueous phase after forming micelles on the LNP surfaces. The assumption was supported by comparing to the foams solely stabilized by CTAB at 27.4 mM, which showed similar foam stability (Fig. 2a and b). For the durable foams stabilized by 2.5 to 10 mg g^{-1} CTAB–LNPs, we further observed the bubble profiles with an optical microscope (OM) and measured the bubble size distributions with dynamic light scatting. The OM images displaced spherical ''cells'' with ruptured shells upon drying of the wet foams, suggesting that the CTAB–LNPs adsorbed at the air–water interface and provided air bubbles with high stability (Fig. S5, ESI†). The average bubble size, along with the uniformity of these bubbles, are summarized in Table 1. We found that the foam stabilized by 5 mg g^{-1} CTAB–LNPs exhibited the narrowest bubble size distribution, ranging from 9 to 80 μm, with an average bubble size of 28 μm and a uniformity of 0.4. At 2.5 mg g^{-1} CTAB–LNPs, the LNPs were likely not sufficiently hydrophobized, while at a CTAB–LNP ratio beyond 5 mg g^{-1}, the LNPs became slightly positively charged and hydrophilic again due to CTAB micelle formation. As a result, the foams stabilized by these particles exhibited a broader bubble size distribution compared to the ones at 5 mg g^{-1} (Fig. 2c). This result is consistent with the foam stability indicated by the change in foaming index over time (Fig. 2b).

Choosing the foam stabilized by 5 mg g^{-1} CTAB–LNPs, we monitored the bubble size distribution for 30 days to evaluate its long-lasting foam stability. It was found that the bubble size did not change over this period (Fig. 2d). This result suggested that the foam was surprisingly stable, with no coalescence or coarsening occurring. Inspired by this excellent foam stability, we selected the same CTAB–LNPs ratio of 5 mg g^{-1} and investigated if these modified LNPs could be used to produce lightweight dry composite foams in combination with CNFs in the next step.

Wet Pickering foams as templates for lightweight composite foams

Direct drying of CTAB–LNP-stabilized Pickering foams led to a collapsed foam structure due to the brittle nature of lignin and the absence of a strong percolation network structure. Our previous study showed that a composite film made of CNFs and LNPs significantly improved the mechanical properties compared to a neat CNF film, due to the synergistic effect of the two nanomaterials.[46] Furthermore, it has been reported that the addition of CNFs to the hydrophobized silica nanoparticles or LNP dispersions significantly improved the Pickering foam/emulsion stability, attributed to the formation of a CNF percolation network structure.[26,49] We thus employed CNFs in our Pickering foam system to enhance both the stability of the wet Pickering foams upon drying and the mechanical properties of the solid foams after drying.

CNF content effect on the dry foam stability. We first examined the effect of CNF amount on the foamability and foam stability of CTAB–LNPs-stabilized foams at a relatively low CNF fraction. We varied the CNF fractions from 1 to 9 wt% (relative to the total solid mass) at the fixed CTAB–LNP concentration of 5 wt%, and observed that the foamability was slightly reduced while foam stability improved with increasing CNF fraction (Fig. S6, ESI†). The trend in foamability is opposite from the findings of Abidnejad *et al.*,[49] who utilized hydrophobized silica nanoparticles as the Pickering particles and a water-ethanol mixture as the liquid phase. The water–ethanol solvent mixture displayed a lower interfacial energy with air and a lower viscosity compared to water and hence the foaming was easier. As a result, the presence of CNFs might facilitate the foamability by enhancing the overall viscosity in their foaming system. We further freeze-dried our CNF-containing foams, and found that the dry foams showed less collapsed foam structures with increased CNF fraction (Fig. S7, ESI†). However, even at 9 wt% CNFs, the dry foam was still brittle, probably due to an insufficient CNF network structure.

To further improve the mechanical properties of the foams after drying, we increased the CNF fraction up to 30 wt%, 40 wt%, and 50 wt% at a fixed CTAB–LNP ratio of 5 mg g^{-1}. The CTAB–LNP concentration was reduced to 1.7 wt%, 1.2 wt% and 0.9 wt%, respectively. The increase in CNF fraction resulted in a reduced foaming index (Fig. 3a), primarily due to both increased viscosity and decreased CTAB–LNP concentration. Nevertheless, all the CNF-containing wet foams exhibited an unchanged foaming index for 30 days. In contrast, the foams stabilized solely with CTAB–LNPs (5 mg g^{-1}) at the concentrations of 1.7 wt%, 1.2 wt% and 0.9 wt% experienced a significant drop in the foaming index after 30 days (Fig. S8, ESI†). Meanwhile, the bubble size distribution of the foams became slightly but not significantly broader with increased CNF fractions (Fig. 3b). Overall, all the wet foams displayed a good distribution of bubble size ranging roughly between 10 and 200 μm.

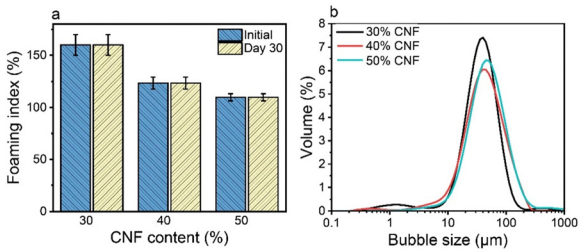

Fig. 3 Foamability and foam stability of the foams stabilized by CTAB–LNPs (5 mg g^{-1}) with the addition of CNFs (30 to 50 wt% relative to the total solid mass). (a) Foaming indices at the initial stage and on day 30. (b) Bubble size distribution of the foams, measured on day 3 after foaming.

Pore morphology of the dry composite foams. Upon freeze-drying, these foams retained their integrity with negligible shrinkage (Fig. 4a, e and j). The SEM images further revealed a honeycomb-like mostly closed-cell structures at the cross-sections of the foams (Fig. 4b, f and j), which are crucial for thermal insulation applications.[50] The dried foams displayed similar cell size distributions roughly between 50–250 μm that were slightly larger than the wet foams (Fig. S9 and S10, ESI†), indicating well-preserved cell structures upon drying. Moreover, the zoomed-in SEM images of the cells and the top surfaces of the foams revealed that, the CNFs were entangled and mostly embedded beneath the CTAB–LNPs (Fig. 4c, d, g, h, k and i). The results suggest that during the drying process, the CTAB–LNPs residing at the air–water bubble interface provided a physical barrier that inhibited bubble coalescence, while CNF network in the aqueous phase enhanced the viscosity and further slowed down coarsening.[26,49]

To validate the SEM observations, we further analyzed the closed-cell contents of the LNP-CNF foams and a commercial rigid PU foam (as comparison) using a pycnometer. The results are listed in Table 2. As anticipated, the closed-cell contents of the LNP-CNF foams dominated the cell structure, and increased from 78.1% to 88.6% with the increased CNF content. This result confirmed that the pore structure could be better preserved upon drying with increased CNF content due to increased viscosity of the system. While comparing the closed-cell contents of the LNP-CNF foams to the rigid PU (97.6%), the highest closed-cell content of the LNP-CNF foam was 9% lower than for PU. This explains partially the better thermal insulation behaviour of the PU foam discussed in the following section. Unfortunately, we could not find the closed/open-cell contents of cellulose/lignin-based foams in the literature for comparison.

Table 2 Apparent density, actual density, and closed-cell contents (eqn (4) and (5)) of the LNF-CNF foams and the reference PU foam

Foam	Apparent density (kg m^{-3})	Actual density (kg m^{-3})	Closed-cell content (%)
30 wt% CNFs	32 ± 3	57	78.1
40 wt% CNFs	34 ± 4	64	85.3
50 wt% CNFs	35 ± 2	66	88.6
Rigid PU	43	85	97.6

Thermal properties of the dry composite foams. The thermal insulation properties of the dry LNP-CNF foams and the rigid PU foam were evaluated using two methods: direct measurement of thermal conductivity and monitoring of surface temperature

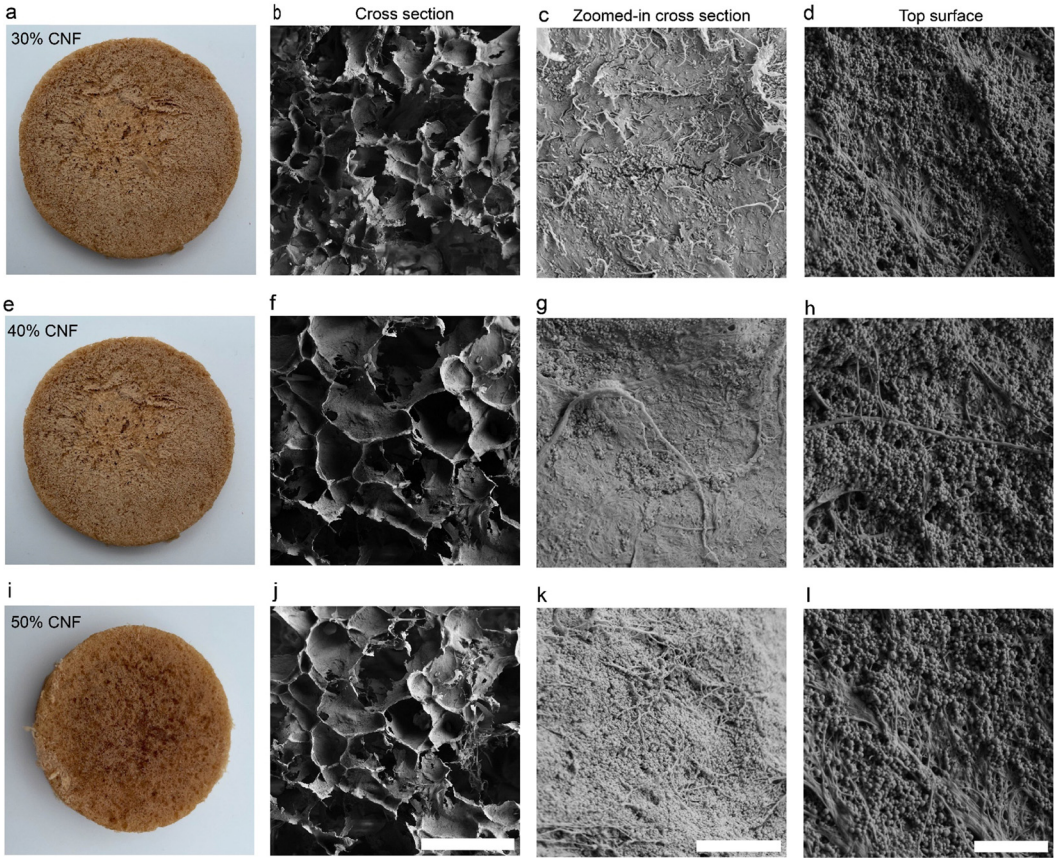

Fig. 4 Macro- and microscopic morphologies of the dry lightweight composite foams comprised of CTAB–LNPs (5 mg g^{-1}) and CNFs at the CNF fractions of 30 wt%, 40 wt%, and 50 wt%, respectively (relative to the total solid mass). (a), (e) and (i) Photos showing the foam appearance. (b), (f) and (j) SEM images of the cross sections of the foams (scale bar: 500 μm). (c), (g) and (k) Zoomed-in SEM images of the cross sections of the foams (scale bar: 1 μm). (d), (h) and (k) SEM images of the foams on the top surfaces (scale bar: 2 μm).

changes by placing the foams on a hot copper plate at 120 °C for 1 hour. The LNP-CNF foams displayed similar thermal conductivities ranging between 0.03 and 0.04 W mK^{-1} (Fig. 5a). These values were about 1.5 times higher compared to the rigid PU foam (0.023 W mK^{-1}), but very close to the expanded polystyrene (EPS) at similar densities.[51,52] While comparing to the foams/aerogels made of various types of CNF, values between 0.014 and 0.086 W mK^{-1} have been reported for the CNF-derived foams/aerogels with a density ranging from 4 to 160 kg m^{-3}.[53] Consistently, the LNP-CNF foams also showed similar surface temperature after being heated on a hot copper plate at 120 °C for 1 hour (Fig. 5a and b). The average surface temperature was about 65 °C for the LNP-CNF foams, and 51 °C for the PU foam (detailed information can be found in Table S3, ESI†). Note that the thickness of the LNP-CNF foams (~10 mm) was about twice higher than the PU foam (5 mm). Overall, the good thermal insulation properties of these foams were ascribed to both the relatively low densities and the mostly closed-cell structures.[54–56]

We further compared the decomposition temperatures of the LNP-CNF foams to the PU foam in a N_2 atmosphere. Overall, the LNP-CNF foams showed similar maximum decomposition temperature at 354 °C, regardless of the CNF content. This value was higher than for the PU foam (335 °C), indicating higher thermal stability of the LNP-CNF foams (Fig. 5c). Interestingly, the LNP-CNF foams yielded less carbon content compared to the PU foam, as indicated by the lower residue weight percentage at 800 °C. Comparing among the LNP-CNF foams with various CNF contents, the more CNF that was added, the lower the carbon content of the foam. This is reasonable, since lignin typically exhibits a higher carbon content compared to cellulose.[57]

Mechanical properties of the dry composite foams. We further examined the compressive stress of these solid foams up to a strain of 80%. Overall, the LNP-CNF foams displayed a gradual increase of compressive stress up to ~30% strain, and a rapid increase thereafter due to densification (Fig. 5d).[49] This stress–strain profile differs from that of the rigid polyurethane (PU) foam, which exhibited a distinct linear elastic region, stress plateau, and densification region (Fig. 5d). Nevertheless, the stress–strain profiles were similar to those reported for foams made of CNFs or refined cellulose pulp.[7,58,59] While comparing the foams containing various amounts of CNFs, an increase in CNF fraction from 30 to 50 wt% resulted in an increase of compressive stress (at 50% strain) and toughness from 31 kPa to 43 kPa and from 28 kJ m^{-3} to 39 kJ m^{-3}, respectively (Table 3). Note that the corresponding specific compressive stress and toughness also increased with the increasing CNF fraction (Table 3). This demonstrates the role of CNF in providing mechanical strength to the foams due to fibril–fibril hydrogen bonding and additional mechanical entanglement. It needs to be emphasized that the compressive stresses at 10% strain and the

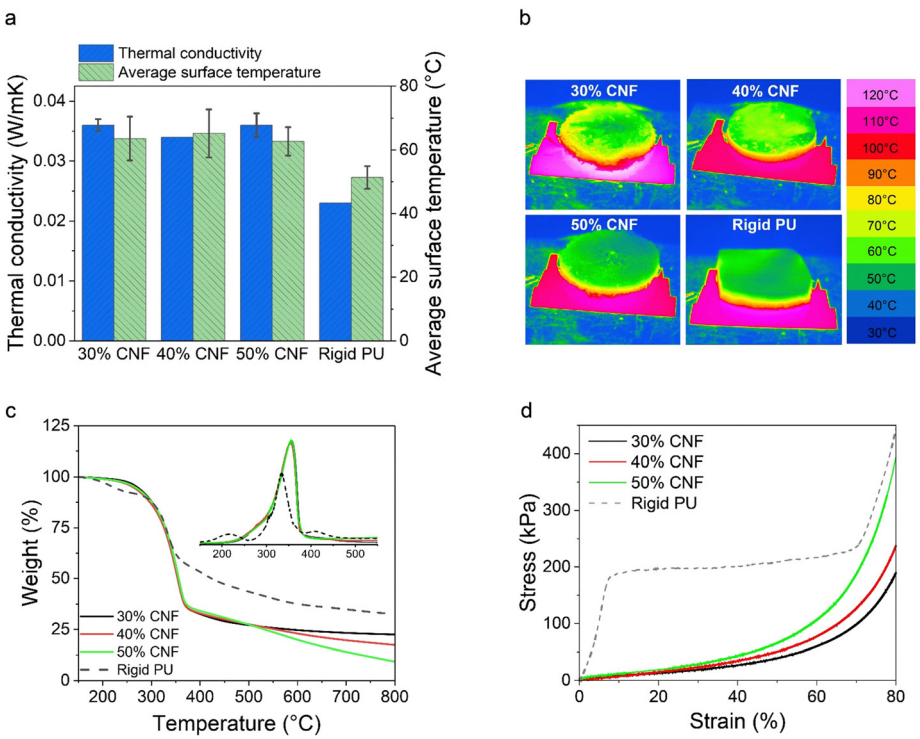

Fig. 5 Thermal and mechanical properties of the dry composite foams comprised of CTAB–LNPs (5 mg g^{-1}) and CNFs at the CNF fractions of 30 wt%, 40 wt% and 50 wt% (relative to the total solid mass), and a commercial rigid PU foam as a reference. (a) Thermal conductivities of the foams measured at room temperature and the average surface temperatures of the foams after being heated on a hot copper plate at 120 °C for 1 hour. (b). Thermal camera images of the foams after being heated on a hot copper plate at 120 °C for 1 hour. (c) The thermal stability of the foams, measured under a N_2 atmosphere. The onset figure shows the first derivative of weight against temperature. (d) Representative compressive stress–strain profiles of the foams up to 80% strain.

Table 3 Mechanical properties of the lightweight LNP-CNF foams and the rigid PU foam

Foam	Compressive stress at 10% strain (kPa)	Compressive stress at 50% strain (kPa)	Toughness (kJ m^{-3})	Specific compressive stress at 10% strain (kPa × m^3 kg^{-1})	Specific compressive stress at 50% strain (kPa × m^3 kg^{-1})	Specific toughness (kJ kg^{-1})
30 wt% CNFs	6.1 ± 3.1	31.3 ± 7.9	28.0 ± 6.5	0.19 ± 0.10	0.98 ± 0.25	0.88 ± 0.20
40 wt% CNFs	5.4 ± 1.3	40.0 ± 8.7	35.4 ± 6.2	0.16 ± 0.04	1.18 ± 0.26	1.04 ± 0.18
50 wt% CNFs	7.6 ± 3.7	43.1 ± 20.0	39.3 ± 21.1	0.22 ± 0.11	1.23 ± 0.57	1.12 ± 0.60
Rigid PU	166.9 ± 45.1	191.2 ± 49.9	155.4 ± 35.4	3.88 ± 1.05	4.44 ± 1.16	3.61 ± 0.82

corresponding specific values did not exhibit statistically significant differences among the various CNF fractions (Table 3). This suggests that CNFs played a more dominant role in stress transfer during the densification stage (strain > 30%) due to disentanglement. Compared with the rigid PU foam, the specific toughness of the best LNP-CNF foam (50 wt% CNF) was about 30% of the value obtained for the PU foam. Future studies should be focused on the improvement of the mechanic strength of the LNP-CNF foams. Nevertheless, the compressive stress of our foams were superior to the results for foams made of carboxylmethylated CNF prepared using a similar strategy but without LNPs.[7,58] This is encouraging since the major component in our foams was the brittle LNPs (50–70 wt%).[40] Furthermore, our compressive stress results were about one magnitude higher compared to foams made of refined cellulose pulp.[59]

Conclusions

In this work, the wettability of LNPs was systematically analyzed over a broad range of concentrations (0–5 wt%) and adsorption ratios of CTAB using DPT. The hydrophobicity of LNPs increased with the LNP concentration due to the protonation of the carboxyl groups. Moreover, the adsorption of CTAB on LNPs could further enhance the hydrophobicity of LNPs. The highest hydrophobicity was achieved when the CTAB–LNPs reached the IEP, as revealed by the highest $|E|$ and the most stable foam stabilized by CTAB–LNPs. At a high LNP concentration (5 wt%) and an adsorption ratio of 5 mg g^{-1} CTAB to LNPs, the achieved Pickering foams were remarkably stable as indicated by the unchanged bubble size distribution over 30 days. The Pickering foams were successfully utilized as templates for making lightweight, strong, and mostly closed-cell foams with the introduction of CNFs. The obtained LNP-CNF foams showed comparable thermal insulation behaviours and better thermal stability compared to a commercial rigid PU foam. The mechanical properties of the dry foams improved with increasing CNF content. The specific toughness of the best LNP-CNF foam (50 wt% CNFs) was about 30% of the value obtained for the rigid PU foam. Overall, our study emphasizes the critical role of interfacial design in leveraging the distinctive properties of lignocellulosic materials for Pickering stabilization in foam applications. By carefully tailoring the interface between the lignocellulosic particles and the surrounding medium, we were able to optimize the stability and performance of the foams. These insights contribute not only to the fundamental understanding of colloidal systems but also offer practical implications for the development of eco-friendly and high-performing foams for applications such as thermal insulation and cushioning.

Author contributions

T. Z. and E. K. designed the experiments with the input from M. Ö. T. Z. performed the particle preparation, surface tension and dilatational viscoelasticity analysis and analyzed the data. E. K. conducted the wet foam and dry foam preparation, characterization, and data analysis. Z. M. and M. A. K. were responsible for the compressive test and the thermal conductivity measurement, respectively. T. Z. and E. K. co-wrote the manuscript with the input from all authors. All authors have given approval to the final version of the manuscript.

Conflicts of interest

The authors declare no competing financial interest.

Acknowledgements

T. Z. acknowledges funding from the MEC Global Program. E. K. acknowledges funding from the Finnish Natural Resources Research Foundation organization in the chemistry – forest product sector under grant number 20210035. We are grateful to Prof. Robin Ras for granting access to the tensiometer at the Department of Applied Physics, Aalto University, and the valuable technical assistance offered by Dr Kai Liu. M.Sc. Senni Heimala was thanked for performing the dynamic foaming analysis (DFA) experiments. This work was mostly performed at Aalto University Bioeconomy Facilities. The authors would also like to acknowledge the OtaNano Nanomicroscopic Center at Aalto University. The authors are also grateful for the support from the FinnCERES Materials Bioeconomy Ecosystem.

References

1 B. P. Binks, *Curr. Opin. Colloid Interface Sci.*, 2002, **7**, 21–41.
2 U. T. Gonzenbach, A. R. Studart, E. Tervoort and L. J. Gauckler, *Langmuir*, 2007, **23**, 1025–1032.
3 E. Dickinson, *Curr. Opin. Colloid Interface Sci.*, 2010, **15**, 40–49.
4 G. Bournival, S. Ata and G. J. Jameson, *Miner. Process. Extr. Metall. Rev.*, 2017, **38**, 366–387.
5 N. Yekeen, M. A. Manan, A. K. Idris, E. Padmanabhan, R. Junin, A. M. Samin, A. O. Gbadamosi and I. Oguamah, *J. Pet. Sci. Eng.*, 2018, **164**, 43–74.

6 U. T. Gonzenbach, A. R. Studart, E. Tervoort and L. J. Gauckler, *J. Am. Ceram. Soc.*, 2007, **90**, 16–22.
7 N. T. Cervin, L. Andersson, J. B. S. Ng, P. Olin, L. Bergström and L. Wågberg, *Biomacromolecules*, 2013, **14**, 503–511.
8 B. P. Binks and T. S. Horozov, *Angew. Chem., Int. Ed.*, 2005, **44**, 3722–3725.
9 U. T. Gonzenbach, A. R. Studart, E. Tervoort and L. J. Gauckler, *Angew. Chem., Int. Ed.*, 2006, **45**, 3526–3530.
10 S. Fujii, P. D. Iddon, A. J. Ryan and S. P. Armes, *Langmuir*, 2006, **22**, 7512–7520.
11 S. Lam, K. P. Velikov and O. D. Velev, *Curr. Opin. Colloid Interface Sci.*, 2014, **19**, 490–500.
12 H. A. Wege, S. Kim, V. N. Paunov, Q. Zhong and O. D. Velev, *Langmuir*, 2008, **24**, 9245–9253.
13 H. Jin, W. Zhou, J. Cao, S. D. Stoyanov, T. B. J. Blijdenstein, P. W. N. de Groot, L. N. Arnaudov and E. G. Pelan, *Soft Matter*, 2012, **8**, 2194–2205.
14 Z. Hu, R. Xu, E. D. Cranston and R. H. Pelton, *Biomacromolecules*, 2016, **17**, 4095–4099.
15 P. Figueiredo, K. Lintinen, J. T. Hirvonen, M. A. Kostiainen and H. A. Santos, *Prog. Mater. Sci.*, 2018, **93**, 233–269.
16 M. H. Sipponen, H. Lange, C. Crestini, A. Henn and M. Österberg, *ChemSusChem*, 2019, **12**, 2039–2054.
17 M. Österberg, M. H. Sipponen, B. D. Mattos and O. J. Rojas, *Green Chem.*, 2020, **22**, 2712–2733.
18 N. Lavoine and L. Bergström, *J. Mater. Chem. A*, 2017, **5**, 16105–16117.
19 N. T. Cervin, E. Johansson, J.-W. Benjamins and L. Wågberg, *Biomacromolecules*, 2015, **16**, 822–831.
20 W. G. Glasser, *Front. Chem.*, 2019, **7**, 565.
21 T. Li and S. Takkellapati, *Biofuels, Bioprod. Biorefin.*, 2018, **12**, 756–787.
22 D. S. Bajwa, G. Pourhashem, A. H. Ullah and S. G. Bajwa, *Ind. Crops Prod.*, 2019, **139**, 111526.
23 D. Kai, M. J. Tan, P. L. Chee, Y. K. Chua, Y. L. Yap and X. J. Loh, *Green Chem.*, 2016, **18**, 1175–1200.
24 M. Österberg, K. A. Henn, M. Farooq and J. J. Valle-Delgado, *Chem. Rev.*, 2023, **123**, 2200–2241.
25 A. Moreno and M. H. Sipponen, *Nat. Commun.*, 2020, **11**, 5599.
26 E. Kimiaei, M. Farooq, R. Grande, K. Meinander and M. Österberg, *Adv. Mater. Interfaces*, 2022, **9**, 2200988.
27 M. H. Sipponen, M. Smyth, T. Leskinen, L.-S. Johansson and M. Österberg, *Green Chem.*, 2017, **19**, 5831–5840.
28 T. Zou, M. H. Sipponen and M. Österberg, *Front. Chem.*, 2019, **7**, 370.
29 M. Ago, S. Huan, M. Borghei, J. Raula, E. I. Kauppinen and O. J. Rojas, *ACS Appl. Mater. Interfaces*, 2016, **8**, 23302–23310.
30 M. Farooq, Z. Tao, J. J. Valle-Delgado, M. H. Sipponen, M. Morits and M. Österberg, *Langmuir*, 2020, **36**, 15592–15602.
31 X. Fan, X. Guan, M. Zhang, Y. Liu and Y. Li, *Colloids Surf., A*, 2022, **643**, 128727.
32 P. Amani, R. Miller, A. Javadi and M. Firouzi, *Adv. Colloid Interface Sci.*, 2022, **301**, 102606.
33 S. Zhang, Q. Lan, Q. Liu, J. Xu and D. Sun, *Colloids Surf., A*, 2008, **317**, 406–413.
34 X. Sun, Y. Chen and J. Zhao, *RSC Adv.*, 2016, **6**, 38913–38918.
35 N. Timmer, D. Gore, D. Sanders, T. Gouin and S. T. J. Droge, *Chemosphere*, 2019, **222**, 461–468.
36 P. Tomani, *Cellul. Chem. Technol.*, 2010, **44**, 53–58.
37 T. Zou, M. H. Sipponen, A. Henn and M. Österberg, *ACS Nano*, 2021, **15**, 4811–4823.
38 M. H. Sipponen, M. Farooq, J. Koivisto, A. Pellis, J. Seitsonen and M. Österberg, *Nat. Commun.*, 2018, **9**, 2300.
39 M. Österberg, J. Vartiainen, J. Lucenius, U. Hippi, J. Seppälä, R. Serimaa and J. Laine, *ACS Appl. Mater. Interfaces*, 2013, **5**, 4640–4647.
40 T. Zou, N. Nonappa, M. Khavani, M. Vuorte, P. Penttilä, A. Zitting, J. J. Valle-Delgado, A. M. Elert, D. Silbernagl, M. Balakshin, M. Sammalkorpi and M. Österberg, *J. Phys. Chem. B*, 2021, **125**, 12315–12328.
41 S. Bhattacharjee, *J. Controlled Release*, 2016, **235**, 337–351.
42 F. Ravera, G. Loglio and V. I. Kovalchuk, *Curr. Opin. Colloid Interface Sci.*, 2010, **15**, 217–228.
43 C. E. Stauffer, *J. Phys. Chem.*, 1965, **69**, 1933–1938.
44 J. Yang, J. Wu and S. Bi, *J. Chem. Eng. Data*, 2021, **66**, 2615–2628.
45 A. Stocco, W. Drenckhan, E. Rio, D. Langevin and B. P. Binks, *Soft Matter*, 2009, **5**, 2215–2222.
46 S. Estravís Sastre, Universidad de Valladolid. Facultad de Ciencias, 2014.
47 B. Kronberg, K. Holmberg and B. Lindman, *Surface Chemistry of Surfactants and Polymers*, John Wiley & Sons, Ltd, 2014, pp. 153–173.
48 S. A. Kedzior, H. S. Marway and E. D. Cranston, *Macromolecules*, 2017, **50**, 2645–2655.
49 R. Abidnejad, M. Beaumont, B. L. Tardy, B. D. Mattos and O. J. Rojas, *ACS Nano*, 2021, **15**, 19712–19721.
50 R. Mort, K. Vorst, G. Curtzwiler and S. Jiang, *RSC Adv.*, 2021, **11**, 4375–4394.
51 B. Doğan and H. Tan, *Int. J. Polym. Sci.*, 2019, **2019**, e6350326.
52 I. Gnip, S. Vėjelis and S. Vaitkus, *Energy Build.*, 2012, **52**, 107–111.
53 V. Apostolopoulou-Kalkavoura, P. Munier and L. Bergström, *Adv. Mater.*, 2021, **33**, 2001839.
54 J. König, A. Lopez-Gil, P. Cimavilla-Roman, M. A. Rodriguez-Perez, R. R. Petersen, M. B. Østergaard, N. Iversen, Y. Yue and M. Spreitzer, *Constr. Build. Mater.*, 2020, **247**, 118574.
55 R. Hasanzadeh, T. Azdast, A. Doniavi and R. E. Lee, *Therm. Sci. Eng. Prog.*, 2019, **9**, 21–29.
56 T. Lohtander, R. Herrala, P. Laaksonen, S. Franssila and M. Österberg, *Cellulose*, 2022, **29**, 1855–1871.
57 T. Haensel, A. Comouth, P. Lorenz, S. I.-U. Ahmed, S. Krischok, N. Zydziak, A. Kauffmann and J. A. Schaefer, *Appl. Surf. Sci.*, 2009, **255**, 8183–8189.
58 S. Y. Park, S. Goo, H. Shin, J. Kim and H. J. Youn, *Cellulose*, 2021, **28**, 10291–10304.
59 J. Liao, P. Luan, Y. Zhang, L. Chen, L. Huang, L. Mo, J. Li and Q. Xiong, *J. Environ. Chem. Eng.*, 2022, **10**, 107788.